JOURNAL OF APPLIED PHYSICS **119**, 085101 (2016)

Electron mean free path in elemental metals

Daniel Gall
Department of Materials Science and Engineering, Rensselaer Polytechnic Institute, Troy, New York 12180, USA

(Received 23 December 2015; accepted 5 February 2016; published online 23 February 2016)

The electron mean free path λ and carrier relaxation time τ of the twenty most conductive elemental metals are determined by numerical integration over the Fermi surface obtained from first-principles, using constant λ or τ approximations and wave-vector dependent Fermi velocities $v_f(\boldsymbol{k})$. The average v_f deviates considerably from the free-electron prediction, even for elements with spherical Fermi surfaces including Cu (29% deviation). The calculated product of the bulk resistivity times λ indicates that, in the limit of narrow wires, Rh, Ir, and Ni are 2.1, 1.8, and 1.6 times more conductive than Cu, while various metals including Mo, Co, and Ru approximately match the Cu resistivity, suggesting that these metals are promising candidates to replace Cu for narrow interconnect lines. © *2016 AIP Publishing LLC*. [http://dx.doi.org/10.1063/1.4942216]

I. INTRODUCTION

The electrical resistivity of metal wires increases as their width decreases.[1–4] This size effect represents a major challenge for nanoelectronics[5] and for the further downscaling of integrated circuits[6,7] as the resistivity of, for example, 10-nm-wide Cu interconnect lines is approximately an order of magnitude larger than that of bulk Cu.[2,8] The primary reason for the resistivity increase is electron scattering at external surfaces and grain boundaries, which are most commonly described by the classical models by Fuchs and Sondheimer (FS)[9,10] and Mayadas and Shatzkes (MS),[11,12] respectively. Both models predict in their approximate form an additive resistivity contribution which is proportional to $\rho_o \times \lambda/d$, where ρ_o and λ are the bulk resistivity and mean free path for electron phonon scattering, and d is the relevant length scale, that is, the wire width or the grain size for surface and grain boundary scattering, respectively. Therefore, in the limiting case of thin wires and/or small grain sizes, the wire resistivity becomes proportional to $\rho_o \times \lambda$ for any given fixed wire dimension and grain size distribution. Thus, the metal with the lowest product $\rho_o \times \lambda$ is expected to exhibit the highest conductivity in the limit of a small wire width. This argument neglects variations in the surface scattering specularity and grain boundary reflection coefficient which are expected to differ for different metals and enter the FS and MS models as phenomenological parameters that also depend on the surface[13–18] and grain boundary[3,19–22] structure and chemistry. Nevertheless, minimizing the product $\rho_o \times \lambda$ is a useful starting point in the focused search for metals that form high-conductivity narrow wires.

Values for the bulk resistivity of elemental metals are well established from measurements at room temperature where electron scattering is dominated by phonons and resistivity contributions due to impurities and crystalline defects are negligible for carefully prepared samples. In contrast, there is only limited information regarding the bulk electron mean free path. One approach is to calculate λ from the measured ρ_o using the free electron model. This assumes a constant Fermi velocity and a spherical Fermi surface, which is a reasonable approximation for alkali and group 11 metals. In fact, the free electron predictions for room temperature Cu and Ag of $\lambda = 39$ and 53 nm are in good agreement with values obtained from fitting the measured resistivity of epitaxial metal layers vs their thickness using the FS model.[14,23,24] In contrast, the limited reported results from metals with non-spherical Fermi surfaces suggest differences by up to an order of magnitude between the λ determined from the free electron model and from fitting resistivity vs thickness data.[25–29] These results are further complicated by anisotropy effects[30–33] and the possible breakdown of the FS model for narrow conductors.[25]

In this paper, I present calculated values of the product $\rho_o \times \lambda$ based on the bulk electronic structure predicted from first-principles density functional calculations. Thus, these calculations correctly account for the anisotropy in the Fermi surface as well as the variation in the electron velocity $\boldsymbol{v}(\boldsymbol{k})$ as a function of wave vector $\boldsymbol{k}$; that is, they go beyond the common effective mass approximation of the FS and MS models that are expected to cause inaccuracies for metals with anisotropic Fermi surfaces. Electron transport is described within a semi-classical Boltzmann transport formalism with individual scattering events that completely randomize the electron momentum, either within a constant mean free path or within a constant mean free time approximation. That is, the electron-phonon scattering probability is approximated by a $\boldsymbol{k}$-independent average distance or average time, respectively. The tabulated results suggest that quite a few (5–10) metals have an effective resistivity that is lower than that of copper in the limit of narrow wires, despite that their bulk resistivity is up to a factor of five larger. Therefore, the decision regarding which of those metals will replace Cu for narrow interconnect lines may ultimately be dominated by secondary factors including processing feasibility and electromigration performance.

II. COMPUTATIONAL APPROACH

The electronic structure of the twenty most conductive elemental metals is obtained from density functional calculations using the Vienna *ab initio* simulation package (VASP), employing periodic boundary conditions, a plane wave basis set, the Perdew-Burke-Ernzerhof generalized gradient approximation (GGA) exchange correlation functional,[34] and the projector-augmented wave method.[35] Computational convergence with respect to the energy cut-off for the plane wave expansion, the k-point grid, and the unit cell size and shape is tested and adjusted such that all values reported in this letter have a computational uncertainty $<1\%$. In addition to the outer-most electron shells, the following electrons are explicitly calculated; that is, they are not included in the core of the pseudo potentials: p for alkali, alkaline earth, and transition metals up to column VI, $4d$ for In, $2s$ and $2p$ for Al, and $1s$ for Be. Calculations are done using primitive unit cells containing one atom for fcc, bcc, and bct and two atoms for hcp structures, and lattice parameters are fixed at the established experimental room temperature values. The latter are typically slightly smaller ($\sim 1\%$) than the values obtained when fitting calculated energy vs lattice parameters, as typical for the generalized gradient approximation.[36] Self-consistent calculations using a Γ-centered $40 \times 40 \times 40$ k-point grid are used to determine the charge distribution, which is subsequently used for non-self-consistent calculations with a finer $200 \times 200 \times 200$ k-point mesh. Such a fine k-point sampling is required for good convergence of the numerical integration across the Fermi surface, which is very sensitive to band crossings. Careful convergence tests are performed for all reported elements to achieve the desired $<1\%$ numerical accuracy, requiring, for example, for Be an increase to $400 \times 400 \times 400$ k-points.

The Fermi surface is determined from the calculated bands, i.e., the calculated electron energy vs $\boldsymbol{k}$ curves $\mathrm{E}_n(\boldsymbol{k})$ where n is the band index. This is done by dividing the Brillouin zone into irregular tetrahedra that are defined by four neighboring k-points. Linear interpolation between the corners yields the intercepts of the Fermi surface with the tetrahedron edges. Three or four intercepts per tetrahedron define one or two triangles of the Fermi surface, respectively,[37] with an electron velocity $\boldsymbol{v}_n(\boldsymbol{k}) = \frac{1}{\hbar}\nabla_k \mathrm{E}_n(\boldsymbol{k})$ that is perpendicular to the triangle surface and is defined by the slope of the band. More elaborate interpolation schemes have been tested, including three-dimensional polynomial interpolation to create k-point submeshes, but do not consistently improve k-point convergence, which is attributed to these approaches being more sensitive to discontinuities at band-crossings.

I reiterate here that all calculations in this paper are done for bulk materials; that is, quantum size effects in narrow wires are not accounted for during the electronic structure calculations. This approximation is justified by the small screening length in metals, resulting in a thin film ballistic conductance that matches the bulk conductance for all but the narrowest layers. For example, a 2-nm-thick Cu layer has a calculated conductance of $0.58 \times 10^{15}\ \Omega^{-1}\ \mathrm{m}^{-2}$ (Ref. 17), in perfect agreement with the bulk value.[38] In contrast, surface roughness in narrow conductors can cause a destruction of isotropic Fermi surface sheets which affects transport properties.[17]

Transport is simulated within a semiclassical approach, such that the bulk conductivity σ_o is given by

$$\sigma_o = \frac{2e^2}{8\pi^3\hbar} \sum_n \iint_{S_F^n} \frac{\tau_n(\boldsymbol{k}) v_{t,n}^2(\boldsymbol{k})}{|\boldsymbol{v}_n(\boldsymbol{k})|} dS. \tag{1}$$

Here, the sum is over bands and the integration is over the Fermi surface S_F^n of band n. The carrier relaxation time $\tau_n(\boldsymbol{k})$, the electron velocity along the transport direction $v_{t,n}(\boldsymbol{k})$, and the electron velocity vector $\boldsymbol{v}_n(\boldsymbol{k})$ are functions of the wave vector $\boldsymbol{k}$ for each band with index n. The factor two in Eq. (1) is accounting for both spins for the case on non-magnetic metals, while this factor is removed for magnetic materials (Co and Ni in this letter) and the contribution from each spin is summed up separately, starting with a spin-polarized density functional calculation.

Using a constant relaxation time approximation, the relaxation time becomes independent of band, spin, and wave vector. That is, $\tau_n(\boldsymbol{k}) = \tau$ and thus

$$\frac{1}{\tau\rho_o} = \frac{e^2}{4\pi^3\hbar} \sum_n \iint_{S_F^n} \frac{v_{t,n}^2(\boldsymbol{k})}{|\boldsymbol{v}_n(\boldsymbol{k})|} dS. \tag{2a}$$

Correspondingly, using a constant mean free path approximation, the carrier relaxation time becomes $\tau_n(\boldsymbol{k}) = \lambda/|\boldsymbol{v}_n(\boldsymbol{k})|$ and therefore

$$\frac{1}{\lambda\rho_o} = \frac{e^2}{4\pi^3\hbar} \sum_n \iint_{S_F^n} \frac{v_{t,n}^2(\boldsymbol{k})}{\boldsymbol{v}_n^2(\boldsymbol{k})} dS. \tag{2b}$$

I note here that for cubic symmetry, the integral in Eq. (2b) is exactly one third of the area of the Fermi surface A_f, such that the product $\lambda \times \rho_o$ is inversely proportional to the Fermi surface area, i.e., $\lambda\rho_o = 12\pi^3\hbar/(e^2 A_f)$ as used, for example, in Ref. 26. This fact is not explicitly used in the numerical code, primarily to keep modularity and flexibility of the computational approach, which first interpolates band energies in the reciprocal coordinate system of the primitive unit cell vectors, second defines the Fermi surface as a list of triangles with associated velocity vectors in a reciprocal Cartesian coordinate system, and third determines transport quantities by summation over all triangles according to Eqs. (2a) and (2b). Integration is done for all calculated metals using multiple transport directions corresponding to conventional [100], [010], [001], [110], $[1\ \bar{1}\ 0]$, and [111] directions. The results are identical within $<1\%$ deviation for all directions for the case of cubic fcc and bcc structures, and for directions within the basal plane for hcp and bct. This is expected based on the 3-dimensional isotropic resistivity for cubic materials and 2-dimensional isotropy within the basal plane of hexagonal and tetragonal symmetries. The values reported, in this letter, are the average from the [100] and [010] directions, while for hcp and bct the [001] values are separately listed.

III. RESULTS AND DISCUSSION

Fig. 1 shows typical Fermi surfaces, in this case, for Cu, Mo, Ru, and Rh. The Brillouin zones are outlined by black

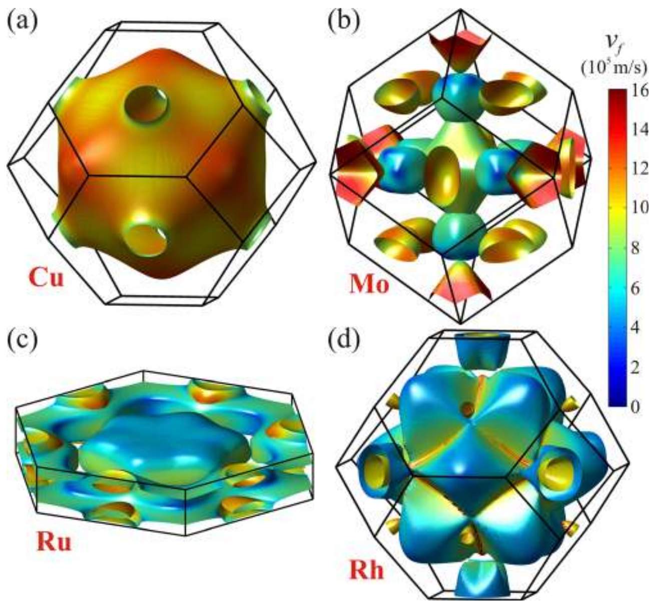

FIG. 1. The Fermi surfaces of (a) Cu, (b) Mo, (c) Ru, and (d) Rh, as obtained from first principles calculations. Colors indicate the Fermi velocity v_f.

lines, while the Fermi surface is colored according to the Fermi velocity $v_f(\boldsymbol{k})$. The Fermi surface of Cu in Fig. 1(a) is nearly spherical, with eight necks that reach along $\langle 111 \rangle$ directions to touch the hexagonal faces of the zone and are due to the reduction of the band energy near the zone boundary.[39] The total Fermi surface area of $2.28 \times 10^{21}\,\mathrm{m}^{-2}$ almost perfectly matches ($<2\%$ deviation) the free-electron prediction of $2.32 \times 10^{21}\,\mathrm{m}^{-2}$. In contrast, the average Fermi velocity of 1.11×10^6 m/s is 29% smaller than the free electron prediction of $v_f = 1.57 \times 10^6$ m/s. The velocity is relatively constant over most of the surface, decreasing from a maximum $v_f = 1.31 \times 10^6$ m/s along $\langle 100 \rangle$ to 1.0×10^6 m/s along $\langle 110 \rangle$, and drops to 0.7×10^6 m/s for the neck at the zone boundary. The Fermi surface for Mo in Fig. 1(b) is $2.55 \times 10^{21}\,\mathrm{m}^{-2}$ and much more complex than for Cu, as multiple 4*d* bands cross the Fermi level in Mo. The Fermi velocity varies by nearly an order of magnitude, from 0.2 to 1.5×10^6 m/s, with an average $v_f = 0.92 \times 10^6$ m/s. More specifically, v_f is 0.8×10^6 m/s for the electron jack near the zone center and decreases continuously to a minimum $v_f = 0.2 \times 10^6$ m/s in the electron knobs that extend along the $\langle 100 \rangle$ directions, $v_f = 0.8$–1.5×10^6 m/s for the hole octahedron and $v_f = 0.9$–1.3×10^6 m/s for the hole ellipsoid near the zone boundary along $\langle 100 \rangle$ and $\langle 110 \rangle$, respectively. The Brillouin zone for Ru in Fig. 1(c) is wider within the basal plane than along the hexagonal axis, reflecting the Ru lattice constants which are 2.706 and 4.282 Å perpendicular and parallel to the hexagonal axis, respectively. The Fermi surface area is $3.32 \times 10^{21}\,\mathrm{m}^{-2}$ and the average $v_f = 0.72 \times 10^6$ m/s. The anisotropy is evident from both the shape and the velocity distribution, with the inner "electron star" exhibiting a relatively low $v_f = 0.3 \times 10^6$ m/s along [0001] but a three times larger $v_f = 0.9 \times 10^6$ m/s within the hexagonal plane while the "hole ring" has $v_f = 0.3$–0.8×10^6 m/s over most of its surface but also exhibits pockets with $v_f = 0.9$–1.2×10^6 m/s which is almost as high as $v_f = 0.9$–1.3×10^6 m/s for the additional separate pockets. The Fermi surface of Rh plotted in Fig. 1(d) is relatively large, $4.73 \times 10^{21}\,\mathrm{m}^{-2}$, and the average velocity small $v_f = 0.67 \times 10^6$ m/s. It exhibits multiple nestled surfaces with both electron and hole character around the zone center and near the zone boundary, respectively. The large Fermi surface of Rh leads to a small product $\lambda \times \rho_o$, which is the smallest of all investigated metals, as discussed below, such that Rh becomes a promising candidate for narrow high-conductivity metal wires.

Table I is a list of the calculated transport data for the twenty most conductive elemental metals. The list is sorted according to increasing bulk resistivity at room temperature $\rho_{o,rt}$, as reproduced from Ref. 40. The values for the average Fermi velocity v_f and the columns $\tau \times \rho_o$ and $\lambda \times \rho_o$ are directly obtained from first principles calculations, using Eqs. 2(a) and 2(b) for the constant τ and λ approximations, respectively. These products are temperature-independent because ρ_o is proportional to the electron-phonon scattering, while τ and λ are inverse proportional to the electron-phonon scattering. The listed values for the room temperature τ_{rt} and λ_{rt} are determined from the $\tau \times \rho_o$ and $\lambda \times \rho_o$ products by dividing by the known room temperature bulk resistivity. Two values are given for hexagonal and tetragonal metals, reflecting transport perpendicular and parallel to the hexagonal/tetragonal axes. That is, the first values are for conduction within the 2-dimensional basal planes and have double the weight in comparison to the second values for conduction in the 3rd dimension. I note here that, for purposes of data consistency, the listed bulk resistivity values are from large-grain randomly oriented polycrystalline samples, even for anisotropic (hcp and bct) metals. Thus, while the calculated data-pairs for $\tau \times \rho_o$ and $\lambda \times \rho_o$ correctly account for the anisotropy in Fermi surface and velocity of hcp and bct metals, the columns for τ_{rt} and λ_{rt} contain two values, which is an artifact of this approach. For example, the calculated $\tau \times \rho_o$ for Mg along the hexagonal axis is 15% smaller than the perpendicular value, indicating a resistivity anisotropy ratio $\rho_{||}/\rho_{\perp} = 0.85$ for Mg. This is in excellent agreement with a reported measured anisotropy value of 0.84.[41] The agreement suggests, since the calculations are done with a constant τ, that the electron-phonon scattering cross-section in Mg is isotropic. Correspondingly, the bulk resistivity could be listed in Table I as two values: $\rho_{\perp} = 4.62\,\mu\Omega$ cm and $\rho_{||} = 3.93\,\mu\Omega$ cm which, in turn, would result in single value for τ_{rt} of 1.86 fs. However, a similar argument within the constant mean free path approximation would yield an anisotropy of 0.90, and therefore slightly different $\rho_{\perp}$ and $\rho_{||}$ values, which would make data presentation in Table I confusing. Moreover, the resistivity anisotropy has not been reported previously for all metals, contains considerable uncertainty with deviations between different reports of up to 30%,[41,42] and also differs considerably (0%–25%) from our calculated anisotropy ratios.[41–44]

Cu has a calculated $\lambda \times \rho_o = 6.70 \times 10^{-16}\ \Omega\,\mathrm{m}^2$, which is within 2% of $6.59 \times 10^{-16}\ \Omega\,\mathrm{m}^2$ determined from the free electron approximation. Correspondingly, $\lambda_{rt} = 39.9$ nm matches the 39 nm reported for room temperature Cu based on the free electron model[2,45] which also matches resistivity-vs-thickness scaling data.[13–15] This agreement between the

TABLE I. List of the twenty most conductive elemental metals, sorted with increasing bulk room-temperature resistivity $\rho_{o,rt}$ from Ref. 40. The average Fermi velocity v_f and the products $\tau \times \rho_o$ and $\lambda \times \rho_o$ are obtained from first principles calculations, while values for the room temperature carrier relaxation time τ_{rt} and mean free path λ_{rt} are obtained by dividing the previous columns by $\rho_{o,rt}$. For hexagonal and tetragonal crystal structures (hcp and bct), the two listed values are for transport perpendicular and parallel to the hexagonal/tetragonal axis.

Element		Crystal structures	$\rho_{o,rt}$ ($\mu\Omega$ cm)	v_f (10^5 m/s)	$\tau \times \rho_o$ (10^{-22} Ω m s)	$\lambda \times \rho_o$ (10^{-16} Ω m^2)	τ_{rt} (fs)	λ_{rt} (nm)
Silver	Ag	fcc	1.587	14.48	5.84	8.46	36.8	53.3
Copper	Cu	fcc	1.678	11.09	6.04	6.70	36.0	39.9
Gold	Au	fcc	2.214	13.82	6.04	8.35	27.3	37.7
Aluminum	Al	fcc	2.650	15.99	3.13	5.01	11.8	18.9
Calcium	Ca	fcc	3.36	4.80	24.7	11.9	73.6	35.4
Beryllium	Be	hcp	3.56	12.62	13.2/21.0	17.1/24.3	37.0/59.1	48.0/68.2
Magnesium	Mg	hcp	4.39	11.63	8.60/7.30	9.81/8.80	19.6/16.6	22.3/20.0
Rhodium	Rh	fcc	4.7	6.67	4.85	3.23	10.3	6.88
Sodium	Na	bcc	4.77	10.21	14.4	14.7	30.2	30.9
Iridium	Ir	fcc	5.2	8.54	4.32	3.69	8.30	7.09
Tungsten	W	bcc	5.28	9.71	8.44	8.20	16.0	15.5
Molybdenum	Mo	bcc	5.34	9.18	6.53	5.99	12.2	11.2
Zinc	Zn	hcp	5.90	15.66	6.80/4.90	10.3/8.1	11.5/8.31	17.4/13.7
Cobalt	Co	hcp	6.2	2.55	13.1/10.9	7.31/4.82	21.2/17.6	11.8/7.77
Nickel	Ni	fcc	6.93	2.34	10.0	4.07	14.5	5.87
Potassium	K	bcc	7.20	7.94	28.6	22.7	39.7	31.5
Cadmium	Cd	hcp	7.5	15.55	8.35/6.89	12.6/11.3	11.1/9.18	16.8/15.1
Ruthenium	Ru	hcp	7.8	7.24	6.88/5.51	5.14/3.81	8.82/7.07	6.59/4.88
Indium	In	bct	8.8	16.32	4.64/4.45	7.62/7.18	5.27/5.05	8.65/8.16
Osmium	Os	hcp	8.9	8.19	7.60/5.51	6.41/4.33	8.54/6.19	7.20/4.87

result from the calculated Fermi surface and a spherical free-electron surface is attributed to a combination of (i) the calculated surface area to be nearly identical to the free-electron area, as discussed above, and (ii) Eq. (2b) for cubic symmetry to be only dependent on the surface area, that is, independent of $\boldsymbol{v}(\boldsymbol{k})$. In contrast, the calculated $\tau \times \rho_o$ of 6.04×10^{-22} Ω m s is 44% larger than the free-electron value of 4.19×10^{-22} Ω m s, reflecting the importance of correctly accounting for $\boldsymbol{v}(\boldsymbol{k})$.

The product $\lambda \times \rho_o$ listed in Table I is interesting for determining the most promising metals for narrow high-conductivity lines, because, based on the FS and MS models, the smallest $\lambda \times \rho_o$ value is expected to yield the lowest resistance in the limit of thin wires with fixed dimension, grain size distribution, and interface scattering cross sections, as discussed above. Various metals have a lower $\lambda \times \rho_o$ product than Cu, which is the metal currently used for interconnects in integrated circuits. Particularly, noteworthy are Rh, Ir, and Ni, with values that are 2.1, 1.8, and 1.6 times smaller than that for Cu, respectively. In addition, metals that have $\lambda \times \rho_o$ values comparable to that of Cu but exhibit either processing and/or electromigration advantages may become competitive as the wire cross-sectional area shrinks. Processing advantages include metals with an established atomic layer deposition process or metals that can be processed through annealing steps to form large grains, reducing the resistivity contribution from grain boundaries. Electromigration advantages primarily refer to metals that exhibit low electromigration such that adhesion/liner/barrier layers may become unnecessary, freeing up space which effectively increases the interconnect cross-sectional area and, in turn, lowers their effective resistivity. Promising metals in that regard are W, Mo, Co, and Ru, all exhibiting $\lambda \times \rho_o$ values within 30% of the value for Cu, despite their 3–5 times larger bulk resistivity.

IV. CONCLUSIONS

The calculated product $\lambda \times \rho_o$ provides guidance in the search for metals that may be suitable for narrow interconnect lines, because the resistance of narrow lines is expected to be proportional to $\lambda \times \rho_o$. The lowest $\lambda \times \rho_o$ is found for Rh, with a value that is 2.1 times smaller than for Cu, potentially yielding narrow lines that are twice as conductive as copper. A whole range of other metals, listed in Table I, also become competitive with Cu in regard to effective conductivity for the limiting case of narrow wires, suggesting that processing viability and electromigration performance will ultimately determine the best metal to replace Cu for integrated circuits.

ACKNOWLEDGMENTS

This research was funded by the Semiconductor Research Corporation under Task 1292.094 and through the STARnet center FAME funded by MARCO, DARPA, and SRC. The author also acknowledges the NSF under Grant No. 1309490. Computational resources were provided by the Center for Computational Innovations at RPI.

[1] J. J. Plombon, E. Andideh, V. M. Dubin, and J. Maiz, Appl. Phys. Lett. **89**, 113124 (2006).

[2] R. L. Graham, G. B. Alers, T. Mountsier, N. Shamma, S. Dhuey, S. Cabrini, R. H. Geiss, D. T. Read, and S. Peddeti, Appl. Phys. Lett. **96**, 042116 (2010).

[3] K. Barmak, A. Darbal, K. J. Ganesh, P. J. Ferreira, J. M. Rickman, T. Sun, B. Yao, A. P. Warren, and K. R. Coffey, J. Vac. Sci. Technol. A **32**, 061503 (2014).

[4] J. S. Chawla, F. Gstrein, K. P. O'Brien, J. S. Clarke, and D. Gall, Phys. Rev. B **84**, 235423 (2011).

[5] M. M. Maqableh, X. Huang, S.-Y. Sung, K. S. M. Reddy, G. Norby, R. H. Victora, and B. J. H. Stadler, Nano Lett. **12**, 4102 (2012).

[6] D. Josell, S. H. Brongersma, and Z. Tőkei, Annu. Rev. Mater. Res. **39**, 231 (2009).

[7] See http://www.itrs.net for International Roadmap Committee, International Technology Roadmap for Semiconductors, 2013.

[8] C. Y. Pan and A. Naeemi, IEEE Electron Device Lett. **35**, 250 (2014).

[9] K. Fuchs, Math. Proc. Cambridge Philos. Soc. **34**, 100 (1938).

[10] E. H. Sondheimer, Adv. Phys. **1**, 1 (1952).

[11] A. F. Mayadas and M. Shatzkes, Phys. Rev. B **1**, 1382 (1970).

[12] A. F. Mayadas, M. Shatzkes, and J. F. Janak, Appl. Phys. Lett. **14**, 345 (1969).

[13] J. S. Chawla, F. Zahid, H. Guo, and D. Gall, Appl. Phys. Lett. **97**, 132106 (2010).

[14] J. S. Chawla and D. Gall, Appl. Phys. Lett. **94**, 252101 (2009).

[15] P. Y. Zheng, R. P. Deng, and D. Gall, Appl. Phys. Lett. **105**, 131603 (2014).

[16] F. Zahid, Y. Q. Ke, D. Gall, and H. Guo, Phys. Rev. B **81**, 045406 (2010).

[17] V. Timoshevskii, Y. Q. Ke, H. Guo, and D. Gall, J. Appl. Phys. **103**, 113705 (2008).

[18] Y. Q. Ke, F. Zahid, V. Timoshevskii, K. Xia, D. Gall, and H. Guo, Phys. Rev. B **79**, 155406 (2009).

[19] J. M. Rickman and K. Barmak, J. Appl. Phys. **114**, 133703 (2013).

[20] T.-H. Kim, X. G. Zhang, D. M. Nicholson, B. M. Evans, N. S. Kulkarni, B. Radhakrishnan, E. A. Kenik, and A.-P. Li, Nano Lett. **10**, 3096 (2010).

[21] M. Cesar, D. P. Liu, D. Gall, and H. Guo, Phys. Rev. Appl. **2**, 044007 (2014).

[22] L. Lu, Y. Shen, X. Chen, L. Qian, and K. Lu, Science **304**, 422 (2004).

[23] J. S. Chawla and D. Gall, J. Appl. Phys. **111**, 043708 (2012).

[24] J. S. Chawla, X. Y. Zhang, and D. Gall, J. Appl. Phys. **110**, 043714 (2011).

[25] D. Choi, X. Liu, P. K. Schelling, K. R. Coffey, and K. Barmak, J. Appl. Phys. **115**, 104308 (2014).

[26] D. Choi, C. S. Kim, D. Naveh, S. Chung, A. P. Warren, N. T. Nuhfer, M. F. Toney, K. R. Coffey, and K. Barmak, Phys. Rev. B **86**, 045432 (2012).

[27] J. S. Chawla, X. Y. Zhang, and D. Gall, J. Appl. Phys. **113**, 063704 (2013).

[28] P. Cotti, E. M. Fryer, and J. L. Olsen, Helv. Phys. Acta **37**, 585 (1964).

[29] G. Brandli and J. L. Olsen, Mater. Sci. Eng. **4**, 61 (1969).

[30] R. Englman and E. H. Sondheimer, Proc. Phys. Soc. London, Sect. B **69**, 449 (1956).

[31] D. Choi, M. Moneck, X. Liu, S. J. Oh, C. R. Kagan, K. R. Coffey, and K. Barmak, Sci. Rep. **3**, 2591 (2013).

[32] P. J. Price, IBM J. Res. Dev. **4**, 152 (1960).

[33] E. Hashimoto and Y. Ueda, J. Phys.: Condens. Matter **10**, 6727 (1998).

[34] J. P. Perdew, K. Burke, and M. Ernzerhof, Phys. Rev. Lett. **77**, 3865 (1996).

[35] J. P. Perdew, J. A. Chevary, S. H. Vosko, K. A. Jackson, M. R. Pederson, D. J. Singh, and C. Fiolhais, Phys. Rev. B **46**, 6671 (1992).

[36] J. Paier, M. Marsman, K. Hummer, G. Kresse, I. C. Gerber, and J. G. Ángyán, J. Chem. Phys. **124**, 154709 (2006).

[37] E. Asier and G. G. Idoia, New J. Phys. **16**, 063014 (2014).

[38] K. M. Schep, P. J. Kelly, and G. E. W. Bauer, Phys. Rev. B **57**, 8907 (1998).

[39] N. Ashcroft and D. Mermin, *Solid State Physics* (Thomson Learning, 1976).

[40] W. M. Haynes, *CRC Handbook of Chemistry and Physics*, 95th ed. (CRC Press, Boca Raton, Fla., 2014).

[41] J. E. A. Alderson and C. M. Hurd, Phys. Rev. B **12**, 501 (1975).

[42] P. Pecheur and G. Toussaint, J. Phys. Chem. Solids **33**, 2281 (1972).

[43] P. G. Tomlinson, Phys. Rev. B **19**, 1893 (1979).

[44] N. V. Volkenshtejn, V. E. Startsev, V. I. Cherepanov, V. M. Azhazha, G. P. Kovtun, and V. A. Elenskij, Fiz. Met. Metalloved. **45**, 1187 (1978).

[45] W. Zhang, S. H. Brongersma, Z. Li, D. Li, O. Richard, and K. Maex, J. Appl. Phys. **101**, 063703 (2007).